Consistent Landmark and Intensity-Based Image Registration

H. J. Johnson* and G. E. Christensen

***Abstract*—Two new consistent image registration algorithms are presented: one is based on matching corresponding landmarks and the other is based on matching both landmark and intensity information. The consistent landmark and intensity registration algorithm produces good correspondences between images near landmark locations by matching corresponding landmarks and away from landmark locations by matching the image intensities. In contrast to similar unidirectional algorithms, these new consistent algorithms jointly estimate the forward and reverse transformation between two images while minimizing the inverse consistency error—the error between the forward (reverse) transformation and the inverse of the the reverse (forward) transformation. This reduces the ambiguous correspondence between the forward and reverse transformations associated with large inverse consistency errors. In both algorithms a thin-plate spline (TPS) model is used to regularize the estimated transformations. Two-dimensional (2-D) examples are presented that show the inverse consistency error produced by the traditional unidirectional landmark TPS algorithm can be relatively large and that this error is minimized using the consistent landmark algorithm. Results using 2-D magnetic resonance imaging data are presented that demonstrate that using landmark and intensity information together produce better correspondence between medical images than using either landmarks or intensity information alone.**

***Index Terms*—Correspondence, deformable templates, image registration, inverse transformation, landmark registration.**

I. Introduction

IMAGE registration algorithms are used to define correspondences between sets of images. Various characteristics of image data are exploited to drive image registration algorithms. The characteristics exploited range from designated landmark positions [1]–[4], to contours [5]–[7] or surfaces [8]–[11], and to volumetric functions of voxel intensities [6], [12]–[21].

There are many image registration algorithms based on the exact matching of corresponding landmarks in two images [22]. The unidirectional landmark thin-plate spline (UL-TPS) image registration technique pioneered by F. Bookstein [1], [2], [23] is the most commonly used landmark driven nonrigid image registration algorithm. Generalizations of UL-TPS procedure include kriging methods [24], [25] that use regularization models other than the TPS model, anisotropic landmark interactions [4] and directed landmarks [26].

Most landmark-based registration algorithms, including the ones described in this paper, assume that a small deformation is sufficient to register a set of images. In cases where the small deformation assumption holds, registration algorithms may efficiently estimate diffeomorphic transformations in a solution space that contain nondiffeomorphic transformations. The small deformation limitation is not universally applicable, and work by Joshi and Miller *et al.* [27]–[29] estimates large deformation transformations in a solution space of diffeomorphisms by constraining the transformations to obey diffeomorphic fluid properties.

The UL-TPS algorithm (see Section II-B) defines a unique smooth registration from a template image to a target image based on registering corresponding landmarks. Correspondence away from the landmark points is defined by interpolating the transformation with a TPS model. Although TPS interpolation produces a smooth transformation from one image to another, it does not define a consistent correspondence between the two images except at the landmark points. This can be seen by comparing the transformation generated by matching a set of template landmarks to a set of target landmarks with the transformation generated by matching the target landmarks to the template landmarks. If the correspondence is consistent then the forward and reverse transformations will be inverses of one another. This is not the case as shown by the examples in Section III. Consistency of the forward and reverse transformations is a necessary condition to define a unique correspondence between two images since it insures that the correspondence defined by the forward transformation is consistent with the correspondence defined by the reverse transformation. Without consistency, the forward transformation would define one correspondence between the images while the reverse transformation would define a different correspondence.

The consistent registration methods presented in this paper builds on the unidirectional landmark and intensity methods described in [30] which used a Fourier series basis to parameterize the transformation and the method developed by Kybic [31] that used B-splines.

In this paper, the idea of consistent image registration [32]–[34], [38] is combined with the UL-TPS algorithm [1]–[4], [23] to overcome the problem that the forward and reverse transformations generated by the UL-TPS algorithm are not inverses of one another. In the consistent image registration approach, the forward and reverse transformations between two images are jointly estimated subject to the constraints that they minimize the TPS bending energy and that they are inverses

Manuscript received November 6, 2001. This work was supported in part by the National Institutes of Health (NIH) under Grant NS35368, Grant DC03590, and Grant CA75731, and in part by a grant from the Whitaker Foundation. *Asterisk indicates corresponding author.*

*H. J. Johnson is with the Electrical and Computer Engineering Department, The University of Iowa Iowa City, IA 52242 USA (e-mail: hans-johnson@uiowa.edu).

G. E. Christensen is with the Electrical and Computer Engineering Department, The University of Iowa Iowa City, IA 52242 USA (e-mail: gary-christensen@uiowa.edu).

Publisher Item Identifier S 0278-0062(02)05530-1.

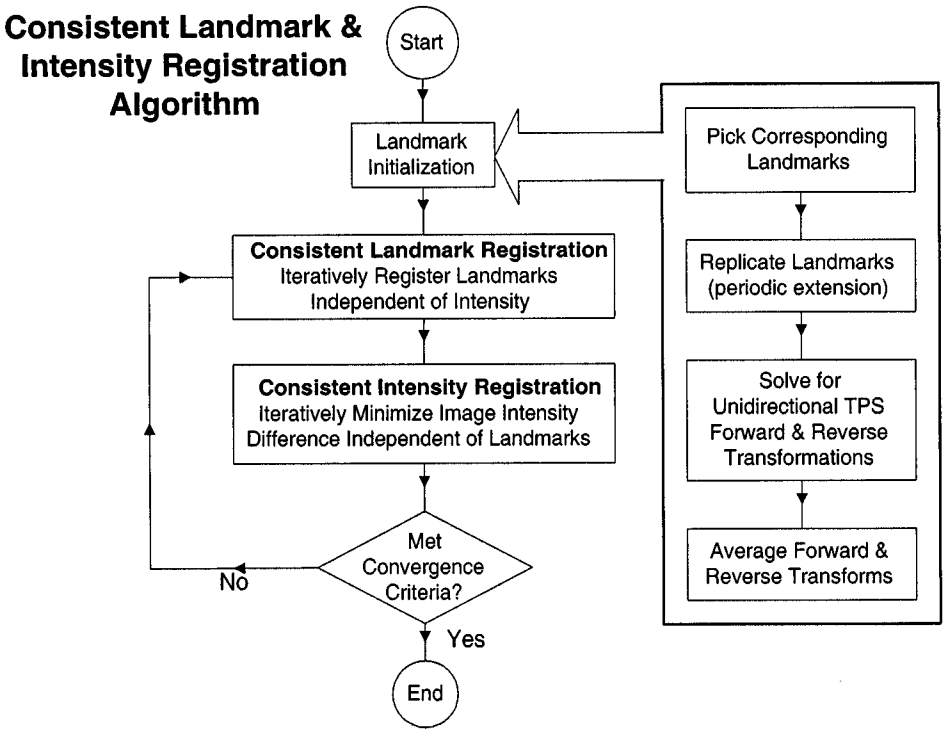

Fig. 1. Flow chart describing the steps of the consistent landmark and intensity image registration algorithm. The images being registered are assumed to be rigidly aligned before starting this procedure.

of one another. The merger of these two approaches produced a consistent landmark-based TPS (CL-TPS) and a consistent landmark- and intensity-based TPS (CLI-TPS) image registration algorithms. The CL-TPS algorithm (see Section II-C) provides a means to estimate a consistent pair of forward and reverse transformations given a set of corresponding points. The CLI-TPS algorithm (see Section II-A) combines both landmark and intensity information to estimate a consistent pair of forward and reverse transformations. The performance of these algorithms are compared using two-dimensional (2-D) magnetic resonance imaging (MRI) brain data images.

II. Methods

A. Consistent Landmark and Intensity-Based Registration

The consistent landmark and intensity image registration algorithm is outlined in Fig. 1. It is assumed that the images being registered have been rigidly rotated and translated to put them into a standard orientation, such as the Talairach coordinate system [35], before applying this procedure. In this paper, the data sets did not need to be scaled to the same size before applying the algorithms since the landmark registration takes care of the global scale differences. The first step of the algorithm is to produce a good initial nonrigid registration using a landmark initialization step. This step consists of: 1) picking corresponding landmarks in the two images; 2) solving the unidirectional TPS algorithm modified to produce periodic boundary conditions for the forward and reverse transformations; and 3) averaging the forward transformation with the inverse of the reverse transformation, and *vice versa*. The full details of the landmark initialization are described in Section II-B.

After the landmark initialization step, the iterative CL-TPS algorithm described in Section II-C is used to produce a consistent set of forward and reverse transformations. This algorithm jointly estimates a set of transformations that minimize both the inverse consistency error and the bending energy of the TPS model while maintaining exact correspondence at the landmarks. The resulting forward and reverse transformations have orders of magnitude less inverse consistency error than the original unidirectional TPS transformations as shown by the experiments in Section III.

The last step of the algorithm is to use the consistent intensity registration algorithm [32]–[34], that is briefly described in Section II-D, to refine the transformations based on matching the intensities of the images. This step matches the images in regions away from the landmarks by minimizing the intensity differences in these regions. The intensity matching does little in regions near corresponding landmarks since these regions have similar intensity patterns that have all ready been matched by the landmark registration. During the intensity matching step, the landmark correspondence error increases in regions where there are bad landmark initializations. The landmark correspondence error also increases in this step due to the TPS regularization model that can pull corresponding landmarks apart. The landmark registration error can be minimized by applying the consistent landmark registration step followed again by the intensity registration step.

The process of alternating between matching the landmarks and then the image intensities is repeated until an appropriate stopping criteria is met. In this work, a fixed number of iterations was used as the stopping criteria. Alternatively, the algorithm could be stopped after an acceptable intensity similarity

and landmark error cost is achieved. The optimal strategy for stopping the algorithm can be quite complex and will be studied in future work.

The consistent landmark and intensity-based TPS algorithm can be thought of as estimating a consistent set of forward and reverse transformations that minimize the intensity differences between two images while being guided by the landmark correspondences. The landmarks guide the solution by initializing the consistent intensity registration algorithm with transformations that are nearly inverse consistent and have exact correspondence at the landmarks. This initialization helps the consistent intensity registration avoid some local minima and, therefore, produce more biologically relevant correspondence maps.

The final registration is determined from the intensity information alone. The landmark matching is used to get the two images close in a global sense and then the intensity information is used to fine tune the registration in the neighborhood of the landmarks. The choice not to use the landmarks for the final registration was motivated by the fact that the landmarks are generally located on object edges or in regions of changing intensity in the image. Therefore, once the landmark matching gets corresponding regions of the images close, the intensity matching finishes the job by matching all of the points in the neighborhood of the landmark based on their intensities.

Another reason that the final registration only used intensity information was that we encountered problems when we tried to force the landmarks and intensity to match at the same time. The problems occured in regions where the landmarks did not correspond to the same location on the intensity profile in both data sets. The Jacobian of the transformation would go negative at the landmark locations when the intensity and landmark forces moved in different directions. This problem was due to the fact that the landmark driving force was focused at the landmark and the intensity driving force was distributed. The Jacobian of the transformation would go negative as the landmark point moved in one direction and the material surrounding the landmark would go in the opposite direction.

The following notation will be used throughout the rest of the paper. The variables q_i and p_i, for $i = 1, \ldots, M$, denote the M corresponding landmarks in the template T and target S images, respectively. The domain of the template image T and target image S is denoted by Ω. The forward transformation $h : \Omega \rightarrow \Omega$ is defined as the mapping that transforms T into the shape of S and the reverse transformation $g : \Omega \rightarrow \Omega$ is defined as the mapping that transforms S into the shape of T. The forward and reverse displacement displacement fields are defined as $u(x) = h(x) - x$ and $w(x) = g(x) - x$, respectively. The inverse of the forward and reverse transformations denoted by $h^{-1}(x)$ and $g^{-1}(x)$, respectively, can be expressed in terms of the displacement fields $\tilde{u}(x) = h^{-1}(x) - x$ and $\tilde{w}(x) = g^{-1}(x) - x$, respectively.

B. Unidirectional Landmark Thin-Plate Spline Registration

The UL-TPS image registration algorithm [1], [2], [23] registers a template image $T(x)$ with a target image $S(x)$ by matching corresponding landmarks identified in both images. Registration at nonlandmark points is accomplished by interpolation such that the overall transformation smoothly maps the template into the shape of the target image.

The unidirectional landmark image registration problem can be thought of as a Dirichlet problem [25] and can be stated mathematically as finding the displacement field u that minimizes the cost function

$$C = \int_{\Omega} \|\mathcal{L}u(x)\|^2 dx \tag{1}$$

subject to the constraints that $u(p_i) = q_i - p_i$ for $i = 1, \ldots, M$. The operator $\mathcal{L}$ denotes a symmetric linear differential operator [36] and is used to interpolate the displacement field u between the corresponding landmarks. When $\mathcal{L} = \nabla^2$, the problem reduces to the TPS registration problem given by

$$C = \int_{\Omega} \|\nabla^2 u(x)\|^2 dx = \sum_{i=1}^{2} \int_{\Omega} \left(\frac{\partial^2 u_i(x)}{\partial^2 x_1} \right)^2 + 2 \left(\frac{\partial^2 u_i(x)}{\partial x_1 \partial x_2} \right) + \left(\frac{\partial^2 u_i(x)}{\partial^2 x_2} \right)^2 dx_1 dx_2 \tag{2}$$

subject to the constraints that $u(p_i) = q_i - p_i$ for $i = 1, \ldots, M$.

It is well known [1], [2], [23] that the TPS displacement field $u(x)$ that minimizes the bending energy defined by (2) has the form

$$u(x) = \sum_{i=1}^{M} \xi_i \phi(x - p_i) + Ax + b \tag{3}$$

where $\phi(r) = r^2 \log r$ and ξ_i are 2×1 weighting vectors. The 2×2 matrix $A = [a_1, a_2]$ and the 2×1 vector b define the affine transformation where a_1 and a_2 are 2×1 vectors. The procedure used to determine these unknown constants is described in Appendix A.

The TPS interpolant $\phi(r) = r^2 \log r$ is derived assuming infinite boundary conditions, i.e., Ω is assumed to be the whole plane R^2. The TPS transformation is truncated at the image boundary when it is applied to an image. This presents a mismatch in boundary conditions at the image edges when comparing forward and reverse transformations between two images. It also implies that a TPS transformation is not a one-to-one and onto mapping between two image spaces. To overcome this problem and to match the periodic boundary conditions assumed by the intensity-based consistent image registration algorithm [32], [34], we use the following procedure to approximate periodic boundary conditions for the TPS algorithm. In the future we plan to replace the following periodic approximation method with an exact solution for the periodic landmark matching. This will be important for extending the algorithm from 2-D to three-dimensional (3-D) since the computation time and storage requirements increase by a factor of 27 for the 3-D case.

It is assumed for all of the algorithms presented in this paper that the images being matched have the same field of view and that they contain the same structures. We further assume that the objects in the images are centered within the image and are padded with the background intensity.

Fig. 2 illustrates the concept of periodic boundary conditions for the landmark TPS registration problem. Cyclic boundary

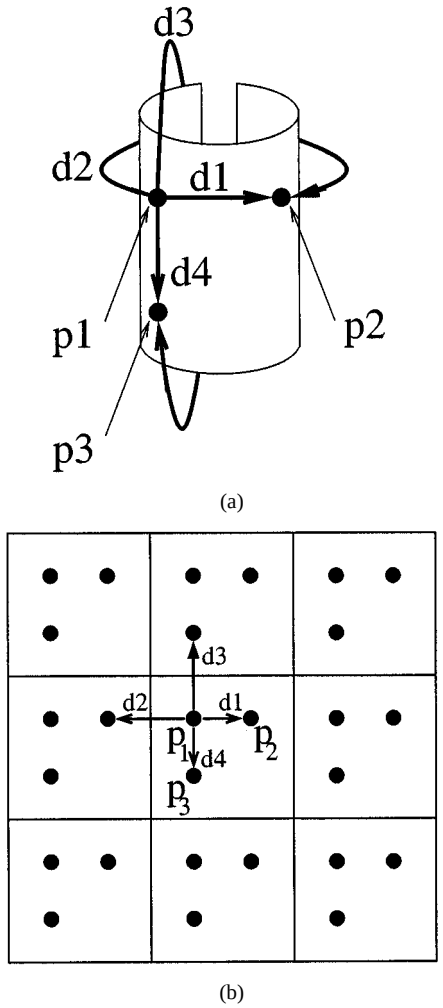

Fig. 2. Diagrams describing the coordinate system and points used to ensure that the resulting displacement field demonstrates continuous periodic boundary conditions. (a) The toroidal coordinate system. (b) The layout of the point used to solve the TPS with approximate circular boundaries.

conditions implies a toroidal coordinate system such that the left–right and top–bottom boundaries of the domain Ω are mapped together. Modifying the boundary conditions in this manner causes an infinite number of interactions between landmarks for a given finite set of landmark points. Fig. 2(b) shows two such interactions between landmark points p_1 and p_2; one within the domain Ω and another between adjacent image domains. We approximate the solution of Laplace's Equation with periodic boundary conditions by solving the TPS registration problem with replicated landmark locations in the eight adjacent domains as shown in Fig. 2(b). This provides a good approximation to periodic boundary conditions since the the kernel function, $\phi(r) = r^2 \log r$, causes interactions between landmarks to decrease rapidly as the distance between landmarks increases. In our tests, there were differences between the transformations found using infinite and periodic boundary conditions but there was nearly no difference in terms of the magnitude of the landmark errors. The major differences between the two sets of boundary conditions was in the location of the maximum inverse consistency error. The maximum inverse consistency error was located on the image boundaries in the case of infinite boundary conditions while it was away from the boundaries for the case of periodic boundary conditions.

The inverse consistency error of the forward and reverse transformations generated by the UL-TPS can be made smaller by averaging the forward transformation with the inverse of the reverse transformation. This averaging will be referred to as the averaged UL-TPS (AUL-TPS) algorithm and is used to initialize the consistent landmark TPS algorithm described in the next section. Note that this procedure does not significantly effect the error at the landmarks since the displacement at the landmark locations in the forward, reverse, inverse-forward, and inverse-reverse transformations are nearly zero as computed by the UL-TPS algorithm.

C. Consistent Landmark Thin-Plate Spline Registration

The AUL-TPS image registration algorithm produces consistent correspondence only at the landmark locations. The CL-TPS image registration algorithm is designed to align the landmark points and minimize the consistency errors across the entire image domain.

The CL-TPS algorithm is solved by minimizing the cost function given by

$$C = \rho \int_\Omega \|\mathcal{L}u(x)\|^2 + \|\mathcal{L}w(x)\|^2 dx + \chi \int_\Omega \|u(x) - \tilde{w}(x)\|^2 + \|w(x) - \tilde{u}(x)\|^2 dx$$

subject to

$$p_i + u(p_i) = q_i \text{ and } q_i + w(q_i) = p_i \text{ for } i = 1, \ldots, M. \tag{4}$$

The first integral of the cost function defines the bending energy of the TPS for the displacement fields u and w associated with the forward and reverse transformations, respectively. This term penalizes large derivatives of the displacement fields and provides the smooth interpolation away from the landmarks. The second integral is called the inverse consistency constraint (ICC) and is minimized when the forward and reverse transformations are inverses of one another. This integral couples the estimation of the forward and reverse transformations together and penalizes transformations that are not inverses of one another. The constants ρ and χ define the relative importance of the bending energy minimization and the inverse consistency terms of the cost function. Notice that this problem is a nonlinear minimization problem since the ICC is a function of the inverse-forward $h^{-1}(x) = x + \tilde{u}(x)$ and inverse-reverse $g^{-1}(x) = x + \tilde{w}(x)$ transformations.

Equation (4) is minimized numerically using the CL-TPS algorithm described in Fig. 3. The algorithm is initialized with the forward and reverse displacement fields u and w either set to zero as in Fig. 3 or with the result of a previous registration algorithm. The temporary variables r_l and s_l are initially set equal to the landmark locations q_l and p_l, respectively, for $l = 1, \ldots M$. The value of r_l converges from q_l to p_l as the algorithm converges and in similar fashion, the value of s_l converges from p_l to q_l.

At each iteration of the algorithm, the UL-TPS algorithm with periodic boundary conditions is used to solve for the perturbation field f_1 that minimizes the distance between the current

Consistent Landmark Thin-plate Spline (CL-TPS) Registration Algorithm

1. Initialization: Set $u(x) = 0$, $w(x) = 0$, $r_l = q_l$, and $s_l = p_l$.
2. Compute $f_1(x)$ that satisfies $\nabla^4 f_1(x) = 0$ subject to $f_1(r_l) = p_l - r_l \quad \forall l$ using the periodic boundary UL-TPS algorithm.
3. Compute $f_2(x)$ that satisfies $\nabla^4 f_2(x) = 0$ subject to $f_2(s_l) = q_l - s_l \quad \forall l$ using the periodic boundary UL-TPS algorithm.
4. Set $u(x) = u(x) + \alpha f_1(x)$ and $w(x) = w(x) + \alpha f_2(x)$.
5. Set $r_l = q_l + u(r_l)$ and $s_l = p_l + w(s_l)$.
6. Compute h^{-1} and g^{-1} using procedure described in [34].
7. Set $\tilde{u}(x) = h^{-1}(x) - x$ and $\tilde{w}(x) = g^{-1}(x) - x$.
8. Set $u(x) = u(x) + \beta[u(x) - \tilde{w}(x)]$ and $w(x) = w(x) + \beta[w(x) - \tilde{u}(x)]$.
9. If the maximum landmark error $|u(q_l) - (p_l - q_l)|$ or $|w(p_l) - (q_l - p_l)|$ is greater than a threshold ϵ_1 or the maximum inverse consistency error $|u(x) - \tilde{w}(x)|$ or $|w(x) - \tilde{u}(x)|$ is greater than a threshold ϵ_2 then Goto 2.

Fig. 3. The CL-TPS algorithm registers two images by matching corresponding landmarks in the images while minimizing the inverse consistency error between the forward and reverse transformations.

position of r_l and its final position p_l. The perturbation field f_1 times the step size α is added to the current estimate of the forward displacement field u where α is a positive number less than one. This procedure is repeated to update the reverse displacement field w. Next, the forward displacement field u is updated with the step size β times the gradient of the ICC with respect to u assuming that $\tilde{w}$ is constant. The displacement field $\tilde{w}$ is computed by taking the inverse of the transformation $g(x) = x + w(x)$ as described in our previous paper describing the consistent intensity registration algorithm [34]. This step is repeated in the reverse direction to update the displacement field $w(x)$. These steps are repeated until the landmark error and the inverse consistency error fall below problem specific thresholds or until a specified number of iterations are reached. In practice, this algorithm converges to an acceptable solution within five to ten iterations and, therefore, we use a maximum number of iterations as our stopping criteria.

D. Consistent Intensity-Based Registration

The consistent intensity-based registration (CI-TPS) algorithm [32]–[34] using TPS regularization is briefly described here. It is based on minimizing the cost function given by

$$\begin{aligned} C =& \sigma \int_\Omega |T(h(x)) - S(x)|^2 + |S(g(x)) - T(x)|^2 dx \\ &+ \rho \int_\Omega \|\mathcal{L}u(x)\|^2 + \|\mathcal{L}w(x)\|^2 dx \\ &+ \chi \int_\Omega \|u(x) - \tilde{w}(x)\|^2 + \|w(x) - \tilde{u}(x)\|^2 dx. \end{aligned} \quad (5)$$

The intensities of T and S are assumed to be scaled between zero and one. The first integral of the cost function defines the cumulative squared error similarity cost between the transformed template $T(h(x))$ and target image $S(x)$ and between the transformed target $S(g(y))$ and the template image $T(y)$. To use this similarity function, the images T and S must correspond to the same imaging modality and they may require preprocessing to equalize the intensities of the image. The similarity function defines the correspondence between the template and target images as the forward and reverse transformations h and g, respectively, that minimize the squared error intensity differences between the images. The second integral is used to regularize the forward and reverse displacement fields u and w, respectively. This term is used to enforce the displacement fields to be smooth and continuous. The third integral is called the ICC and is minimized when the forward and reverse transformations h and g, respectively, are inverses of each other. The constants σ, ρ and χ define the relative importance of each term of the cost function.

The cost function in (5) is discretized to numerically minimize it. The forward and reverse transformations h and g and their associated displacement fields u and w are parameterized by the discrete Fourier series defined by

$$\begin{aligned} u_d[n] &= \sum_{k \in \Omega_d} \mu[k] e^{j\langle n, \theta[k] \rangle} \quad \text{and} \\ w_d[n] &= \sum_{k \in \Omega_d} \eta[k] e^{j\langle n, \theta[k] \rangle} \end{aligned} \quad (6)$$

for $n \in \Omega_d$ where the basis coefficients $\mu[k]$ and $\eta[k]$ are (2×1) complex-valued vectors and $\theta[k] = [(2\pi k_1)/N_1, (2\pi k_2)/N_2]^T$. The basis coefficients have the property that they have complex conjugate symmetry, i.e., $\mu[k] = \mu^*[N - k]$ and $\eta[k] = \eta^*[N - k]$. The notation $\langle \cdot, \cdot \rangle$ denotes the dot product of two vectors such that $\langle n, \theta[k] \rangle = (2\pi k_1 n_1)/N_1 + (2\pi k_2 n_2)/N_2$. The basis coefficients $\mu[k]$ and $\eta[k]$ of the discretized forward and reverse displacement fields are then minimized using gradient descent as described in [32] and [34].

The intensity similarity component of the cost function is forced to register the global intensity patterns before local intensity patterns by restricting the similarity gradient to modify only the low frequencies of the displacement field parameters. Restricting the similarity cost gradient to modifying the low-frequency components is analogous to filtering with a zonal low-pass filter. To mitigate the Gibbs ringing associated with zonal low-pass filters, a low-pass Butterworth filter is applied to the similarity cost gradient in the gradient decent algorithm.

E. Appending the Consistent Landmark and Intensity Registration Algorithms

The parameterization of the transformations used in the consistent landmark (CL-TPS) algorithm and the consistent intensity (CI-TPS) algorithm are different. A spatial sampling param-

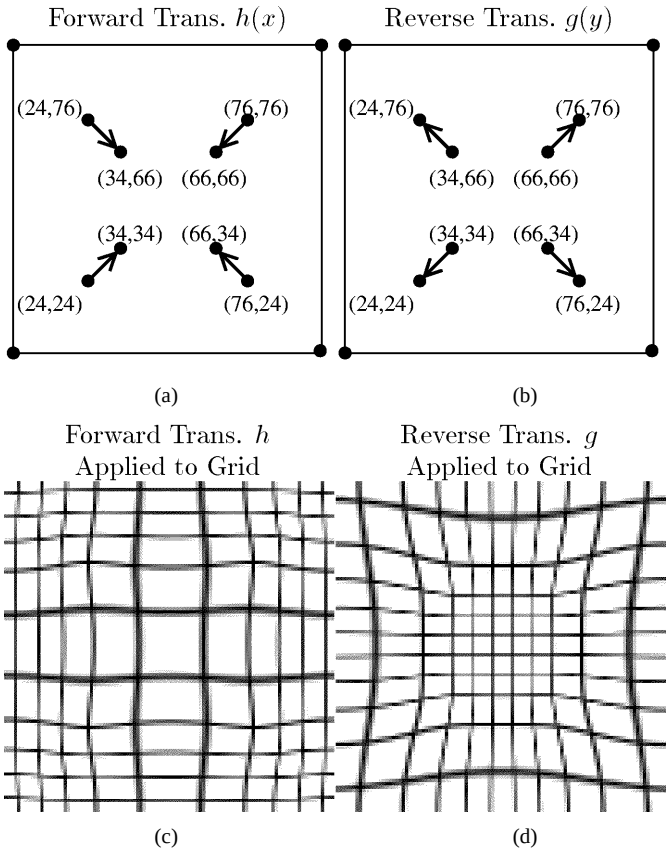

Fig. 4. The location of local displacements at the landmarks points for the forward, and reverse transformations of images with 100×100 pixels. Application of the TPS deformation fields to uniformly spaced grids for the forward and reverse transformations.

eterization of the displacement field is used in the CL-TPS algorithm while a Fourier series parameterization of the displacement field is used in the CI-TPS algorithm. The parameterization used in one algorithm must be converted into the parameterization of the other in order to use the result from one algorithm to initialize the other as outlined in the CLI-TPS algorithm defined in Fig. 1. This is accomplished by using the fast Fourier transform (FFT) and the inverse FFT (IFFT) to convert the spatial representation of the displacement field to the Fourier Series representation and *vice versa*.

III. Results

A. Landmark Registration

The first experiment compares the inverse consistency error associated with the traditional UL-TPS algorithm to that of the consistent landmark CL-TPS algorithm. This simple experiment is designed to show that the UL-TPS algorithm can have significant inverse consistency error while this error is minimized using the CL-TPS algorithm. The experiment shown in Fig. 4 consisted of matching eight landmarks in one image to their corresponding landmarks in a second image using both the UL-TPS and the CL-TPS algorithm. The arrows in Fig. 4(a) and (b) shows the displacement between the corresponding landmarks in the forward and reverse directions, respectively. The four landmarks in the corners of the images were fixed. The forward transformation h maps the four inner points to the four outer points and the reverse transformation g maps the outer points to the inner points. Applying the CL-TPS transformations to a rectangular grid shows that the forward transformation—defined with respect to a Eulerian frame of reference—causes the center of the image to expand [Fig. 4(c)] while the reverse transformation causes a contraction of the central portion of the image [Fig. 4(d)].

The top row of Fig. 5 shows the spatial locations and magnitudes of the inverse consistency errors of the forward and reverse transformations generated by the UL-TPS algorithm. The images in the left column were computed by taking the Euclidean norm of the difference between the forward transformation h and the inverse of the reverse transformation g^{-1}. The images in the center column were computed in a similar fashion with g and h^{-1}. The CL-TPS result was created using AUL-TPS initialization and minimizing for 100 iterations with $\alpha = 0.5$ and $\beta = 0.012$. This registration took approximately 3 min on a single 667-MHz alpha processor.

The tables in Fig. 5 tabulate the inverse consistency error at four representative points in the images. The points A and C are located at points away from landmarks while the points B and D are located at landmark locations. The inverse consistency error at the landmark points is small for both algorithms. However, the landmark error is quite large away from the landmark locations in the UL-TPS algorithm. The range of intensities on the color bar for each method shows that the range of inverse consistency errors for the UL-TPS algorithm was in the range of 0.002 to 4.9 pixels while this same error for the CL-TPS algorithm ranged from 0.00 to 0.009. This shows that the CL-TPS algorithm reduced the inverse consistency error by over 500 times that of the UL-TPS algorithm for this example.

A pair of transformations are point-wise consistent if the composite function $h(g(x))$ maps a point x to itself. Spatial deviations from the identity mapping can be visualized by applying the composite mapping to a uniformly spaced grid. The grid is deformed by the composite transformation in regions where the forward and reverse transformations have inverse consistency errors. The composite transformation does not deform the grid for a perfectly inverse consistent set of forward and reverse transformations. Fig. 6 shows the composite mapping produced by the UL-TPS [Fig. 6(a)] and the CL-TPS [Fig. 6(b)] applied to a rectangular grid for this experiment. Notice that there is a considerable amount of inverse consistency error in the UL-TPS algorithm while there is no visually detectable inverse consistency error produced by the CL-TPS algorithm. The blurring of the grid is due to bilinear interpolation used to deform the grid images with the error displacements. Both images are created with the same technique, but the inverse consistent image needs very little interpolation since there is nearly zero displacement error.

The minimum and maximum Jacobian values of the forward (reverse) transformation specify the maximum expansion and contraction of the transformation, respectively. The Jacobian error (JE), calculated as $1/2|\min\{Jac(h)\} - 1/\max\{Jac(g)\}| + 1/2|\min\{Jac(g)\} - 1/\max\{Jac(h)\}|$, provides an indirect measure of the inconsistency between the forward and reverse transformations. The JE is zero if the forward and reverse transformations are inverses of one

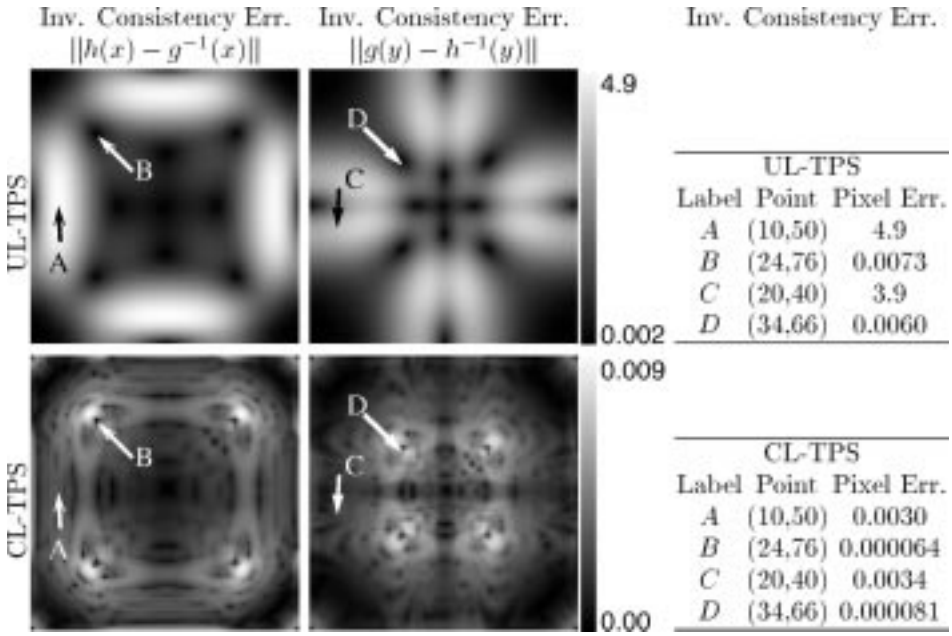

UL-TPS

Label	Point	Pixel Err.
A	(10,50)	4.9
B	(24,76)	0.0073
C	(20,40)	3.9
D	(34,66)	0.0060

CL-TPS

Label	Point	Pixel Err.
A	(10,50)	0.0030
B	(24,76)	0.000064
C	(20,40)	0.0034
D	(34,66)	0.000081

Fig. 5. The left and center panels show the inverse consistency errors of the forward and reverse transformations, respectively. The tables in the right columns list the landmark errors associated with selected image points. The top and bottom rows are the inverse consistency errors associated with the UL-TPS and CL-TPS landmark algorithms, respectively.

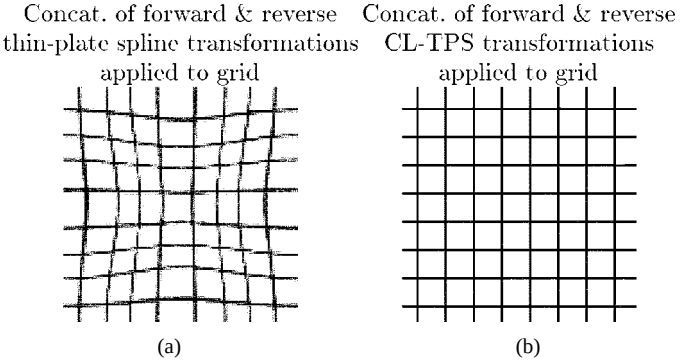

Fig. 6. Deformed grids showing the error between the forward and reverse transformations estimated with (a) the landmark-based TPS algorithm and (b) the CL-TPS algorithm. The grids were deformed by the transformation constructed by composing the forward and reverse transformations together, i.e., $g(h(x))$. Ideally, the composition of the forward and reverse transformations is the identity mapping which produces no distortion of the grid as in (b). The fuzziness associated with the grids are due to the bilinear interpolation.

another, but the converse is not true. Table I shows that the JE was 1000 times smaller for the CL-TPS algorithm compared with the UL-TPS algorithm.

B. Landmark and Intensity Registration

The five 2-D transverse MRI data sets shown in Fig. 7 were used to compare the performance of the UL-TPS, CL-TPS, CI-TPS, and consistent landmark and intensity TPS (CLI-TPS) algorithms. These 256×320 pixel images with 1 millimeter isotropic pixel dimension were extracted from 3-D MRI data sets such that they roughly corresponded to one another. Each data set was registered with the other four data sets for each of the four algorithms producing ten forward and reverse transformations for each algorithm. For brevity of presentation, we only present some of the results of the experiments that are representative of all of the results. A set 39 of corresponding

TABLE I
COMPARISON BETWEEN THE UL-TPS, AUL-TPS, AND CL-TPS IMAGE REGISTRATION ALGORITHMS. THE TABLE COLUMNS ARE THE EXPERIMENT, (ICC), TRANSFORMATION DIRECTION (TD), AVERAGE LANDMARK ERROR (ALE) IN PIXELS, MAXIMUM LANDMARK ERROR (MLE), MAXIMUM INVERSE ERROR (MIE) IN PIXELS, AVERAGE INVERSE ERROR (AIE) IN PIXELS, MINIMUM JACOBIAN (MJ) VALUE, INVERSE OF THE MAXIMUM JACOBIAN VALUE (IJ), AND JE

Experiment	ICC	TD	ALE	MLE	AIE	MIE	MJ	IJ	JE
UL-TPS	No	Forward	0.010	0.016	2.2	4.1	2.4	4.8	1.4
		Reverse	0.0056	0.010	2.0	4.9	2.9	3.2	
AUL-TPS	No	Forward	0.0074	0.013	0.091	0.20	0.28	0.47	0.011
		Reverse	0.0072	0.012	0.082	0.29	0.45	0.27	
CL-TPS	Yes	Forward	0.00055	0.0011	0.0028	0.0078	0.28	0.48	0.0012
(100 iter.)		Reverse	0.00046	0.00094	0.0024	0.0088	0.48	0.28	

landmarks were manually defined in data sets $B2$ and $B4$ and a subset of the 39 landmarks were manually defined in the additional three data sets (see Fig. 7). Only data sets $B2$ and $B4$ had all 39 landmarks identified on them since it was not possible to locate the corresponding locations for all the landmarks on the other data sets due to missing or different shaped sulci. Only corresponding landmarks between two images were used for registration and calculating the landmark error, i.e., if one image set was missing landmark 15, then landmark 15 was not used for registration or for calculating the landmark error.

Table II lists the parameters used for each algorithm and the computation time that each algorithm required to run on a single 667-MHz alpha processor. The algorithmic parameters were chosen to demonstrate the registration performance of the algorithms independent of optimizing the run times. These computation times can be decreased significantly by optimizing the computer code and reducing the number of iterations. The CLI-TPS algorithm was run for five iterations of the CL-TPS registration algorithm followed by 95 iterations of the CI-TPS registration algorithm.

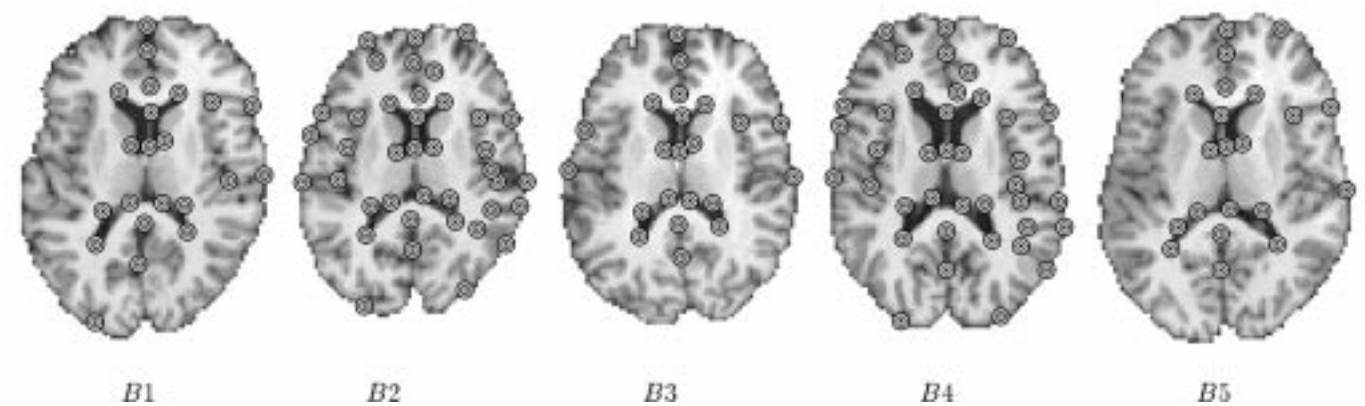

Fig. 7. Five corresponding image slices from MRI acquired brains with manually identified points of correspondence.

TABLE II
SUMMARY OF ALGORITHM PARAMETERS AND COMPUTATION TIMES ON A SINGLE 667-MHZ ALPHA PROCESSOR

Algorithm	Iterations	Computation Time	χ	ρ	σ	α	β
UL-TPS	1	5 seconds	NA	NA	NA	NA	NA
CL-TPS	20	3 minutes	NA	NA	NA	1.0	0.0061
CI-TPS	1000	1 hour	500	0.0000075	0.10	NA	NA
CLI-TPS	300	1 hour	500	0.0000075	0.50	1.0	0.0061

The result of transforming MRI data set $B5$ in to the shape of $B2$ using each of the four registration algorithms is shown in Fig. 8. These results are typical of the other pairwise registration combinations. The images are arranged left to right from the worst to the best similarity match as shown by the corresponding difference images shown below the transformed images. The UL-TPS and CL-TPS algorithms perform almost identically with respect to similarity matching. The CI-TPS and CLI-TPS intensity-based registrations produce better similarity match than the two landmark only methods. In particular, the intensity-based methods match the border locations and non-landmark locations better than the landmark TPS or CL-TPS algorithms. The difference between the CI-TPS and CLI-TPS methods is that the CLI-TPS method produces much smaller landmark errors than the CI-TPS method which cannot be seen in the intensity difference images.

The images in Fig. 9 show the Jacobian of the forward and reverse transformations between images $B2$ and $B1$ produced by the CL-TPS[Fig. 9(a) and (b)] and CLI-TPS [Fig. 9(c) and (d)] algorithms, respectively. The value of the Jacobian at a point is encoded such that bright pixels represent expansion, and dark pixels represent contractions. Notice that the intensity pattern of the forward and reverse Jacobian images appear nearly opposite of one another since expansion in one domain corresponds to contraction in the other domain. These images show the advantage of using both landmark and intensity information together as opposed to just using landmark information alone. Notice that the CL-TPS algorithm has very smooth Jacobian images compared with the CLI-TPS algorithm. This is because the CL-TPS algorithm matches the images at the corresponding landmarks and smoothly interpolates the transformation between the landmarks. Conversely, the patterning of the local distortions in the CLI-TPS registration resemble the underlying intensity patterning. This indicates that combining the intensity information with the landmark information provides additional local deformation as compared with using the landmark information alone. This improved registration between landmarks produces more distortion of the template image and, therefore, there is a larger range of Jacobian values for the CLI-TPS algorithm than the CL-TPS algorithm as shown by the color bar scales.

Inverse consistency error images are computed by taking the Euclidean norm of the difference between the forward and the inverse of the reverse transformations at each voxel location in the image domain. Fig. 10 shows the inverse consistency error images for the registration of data sets $B2$ and $B5$ using the UL-TPS, CL-TPS, CI-TPS, and and CLI-TPS algorithms. Note that each images is on its own color-scale and that the UL-TPS algorithm has 10–200 times more maximum inverse consistency error than the consistent registration algorithms. The UL-TPS algorithm had 50–500 times more average inverse consistency error than the consistent registrations algorithms. This can be seen by comparing large regions of bright pixels in the UL-TPS image to the small regions of bright pixels in the other images. This figure shows that consistent registration algorithms produced forward and reverse transformations that had subvoxel inverse consistency errors at all voxel locations. The inverse consistent errors in the UL-TPS and CL-TPS algorithms are greatest away from the landmark driving forces because the landmark driving forces are implicitly inverse consistent. The largest inverse consistency errors in the CI-TPS and CLI-TPS algorithms occur near edges where there is a correspondence ambiguity associated with the intensity matching solution.

Fig. 11 shows plots of the intensity similarity cost, landmark error cost, and the maximum inverse consistency error costs as a function of iteration for CLI-TPS registration of data sets $B2$ and $B4$. The protocol used for this experiment was five iterations of the CL-TPS algorithm followed by 95 iterations of the CI-TPS algorithm. The intensity similarity cost decreases during the CI-TPS algorithm when the intensity is being matched and increases during the CL-TPS algorithm as the landmarks are matched. Conversely, the landmark error decreases during the CL-TPS algorithm and increases during CI-TPS algorithm as the intensity is matched. The plot of the maximum inverse consistency error shows that switching from the intensity (CI-TPS) to the landmark (CL-TPS) algorithm causes a jump in the inverse consistency error which is quickly minimized. We observed that smaller landmark and intensity

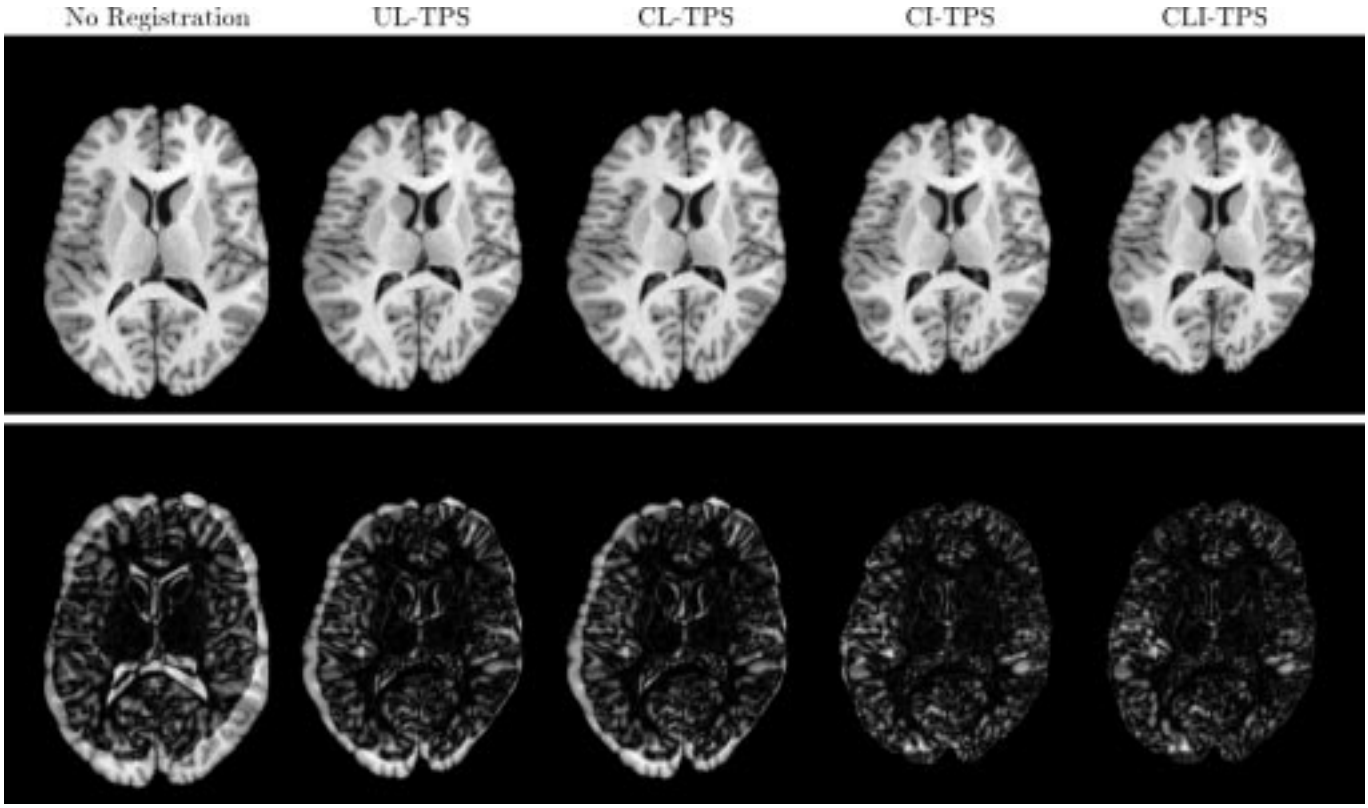

Fig. 8. Intensity matching results for registering dataset $B5$ to dataset $B2$ with the four registration algorithms. The top row shows the data set $B5$ transformed into the shape of $B2$ using each algorithm and the bottom row shows the absolute difference image between the transformed $B5$ image and the target $B2$ image. Note that the intensity difference images of the CI-TPS and CLI-TPS are very similar since both algorithms minimize the intensity differences between the deformed template and target images. However, the difference between these two results is that the CLI-TPS also produces much smaller landmark errors which cannot be seen in the intensity difference images.

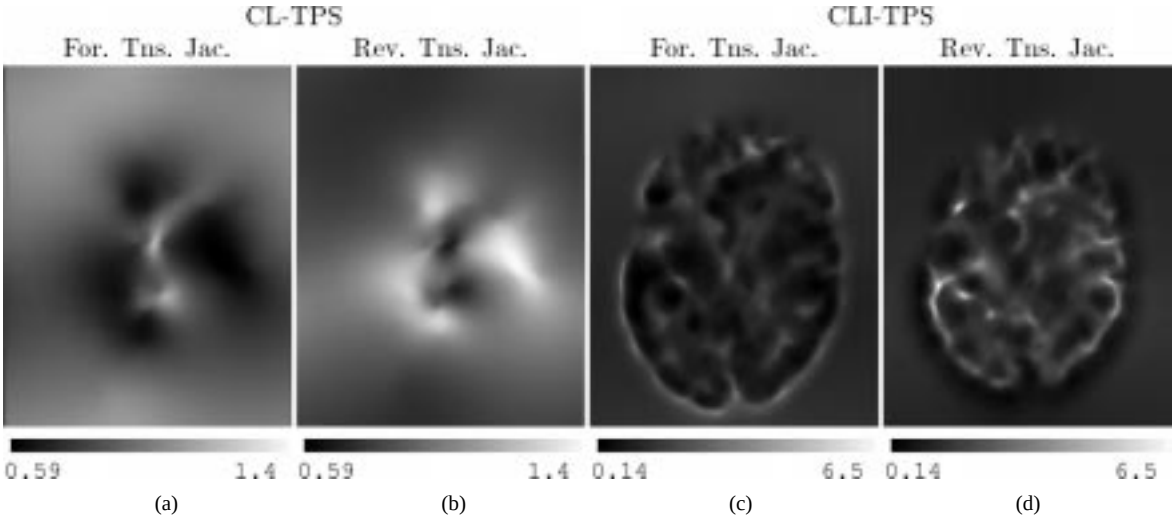

Fig. 9. This figure shows the Jacobians of the forward and reverse transformations for the registration of data sets $B2$ and $B1$ for the CL-TPS [(a) and (b)] and CLI-TPS [(c) and (d)] algorithms. The bright pixels of the Jacobian images represent regions of expansion and dark pixels represent regions of contraction.

error is achieved by the CLI-TPS in one-third of the number of iterations than by either CI-TPS or CL-TPS alone.

Fig. 11(c) shows the minimum and maximum Jacobian values of the forward and reverse transformations as a function of iteration. These plots show that the ICC causes the minimum Jacobian value of the forward transformation to track with the inverse of the maximum Jacobian value (IJ) of the reverse transformation and *vice versa*. Note that these plots give an upper bound on the inverse consistency error since the minimum and maximum Jacobian values of the forward and reverse transformations do not correspond to the same points.

Table III summarizes the representative statistics collected from the experiments. Comparing the results of the UL-TPS and CL-TPS algorithms shows that the addition of ICC improved the inverse consistency of the transformations with no degradation of the landmark matching. Note that for the UL-TPS algorithm,

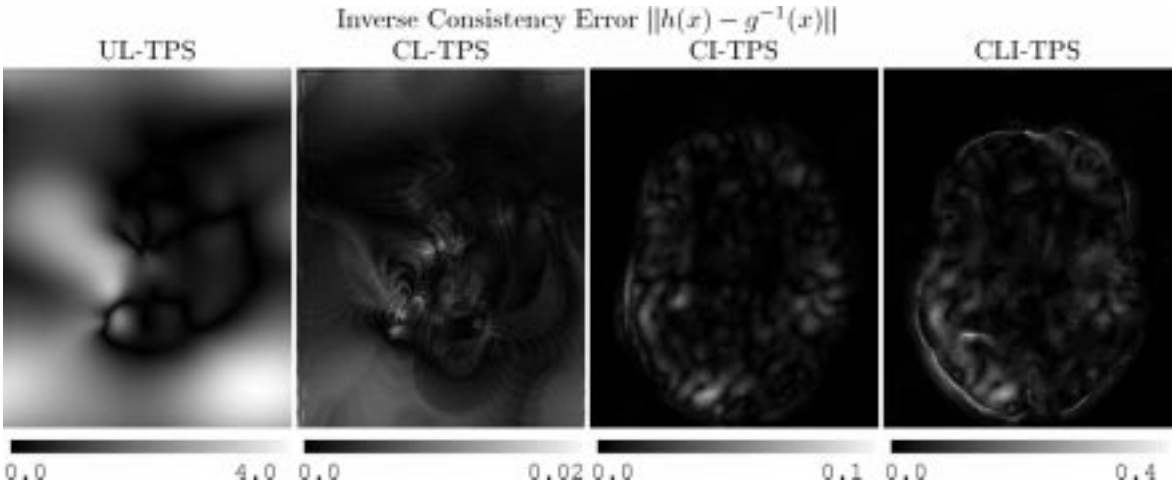

Fig. 10. Images that display the magnitude and location of forward transformation inverse consistency errors for matching data sets $B2$ and $B5$ with UL-TPS, CL-TPS, CI-TPS, and CLI-TPS registration algorithms.

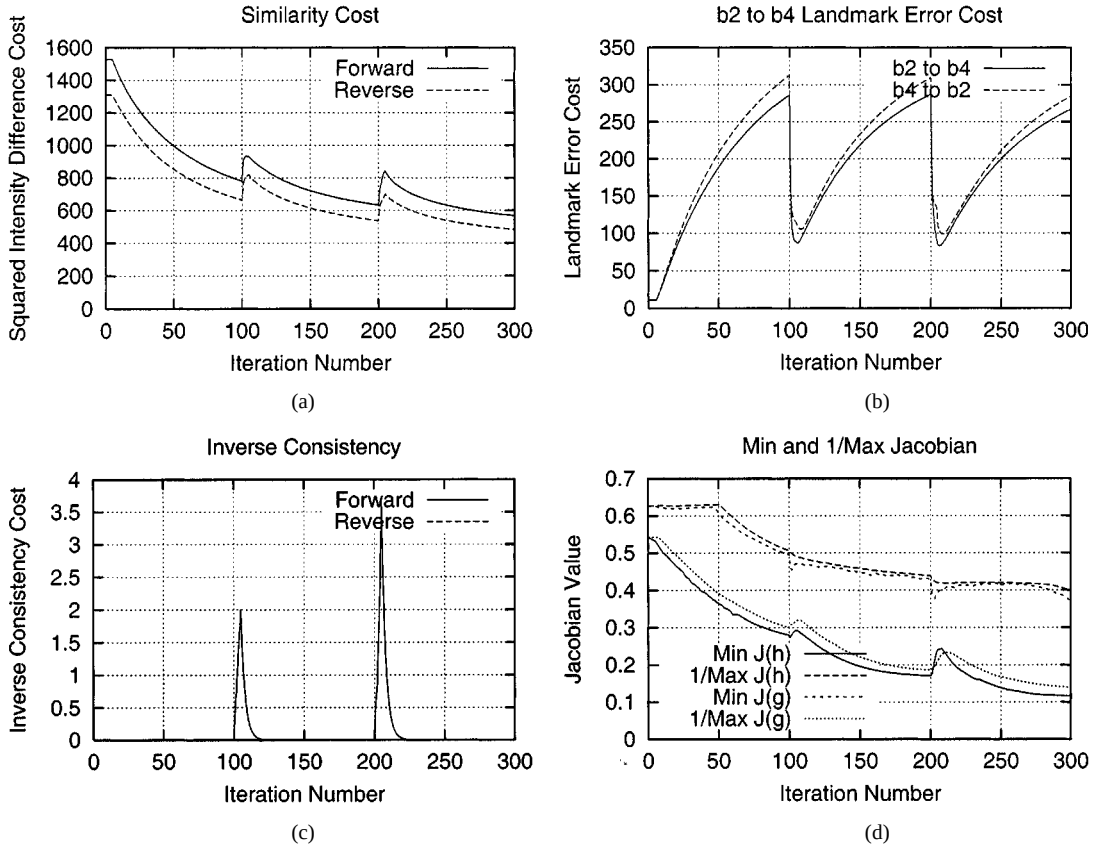

Fig. 11. Plots of the intensity and landmark costs as a function of iteration for the CLI-TPS registration of data sets $B2$ and $B4$.

the inverse consistency error tends to be be larger as one moves away from landmarks and that the inverse consistency error can be decreased by defining more corresponding landmarks.

Table III also demonstrates that the CI-TPS and CLI-TPS registrations have a smaller average intensity difference but larger landmark errors. The CLI-TPS has smaller average intensity difference and smaller landmark errors than the CI-TPS registration algorithm. The CLI-TPS algorithm produces a better similarity match because the landmark driving force pulls the intensity driving function out of local minima. It should be noted that the large number of landmarks used in the CLI-TPS registration limits the effect of the intensity driving force in neighborhoods of the landmarks. In practice, when the the landmark points are more sparse the intensity driving force plays a more important role.

IV. Summary and Conclusion

This work presented two new image registration algorithms based on TPS regularization: landmark-based CL-TPS image

TABLE III
EXPERIMENTAL RESULTS PRODUCED BY MAPPING MRI BRAIN IMAGE 2 INTO IMAGES 1, 3, 4, AND 5 (SEE FIG. 7). THE TPS ALGORITHMS COMPARED IN THIS TABLE ARE THE UL-TPS, AUL-TPS, CL-TPS, CI-TPS, AND CLI-TPS ALGORITHMS. THE STATISTICS COMPUTED FOR THESE EXPERIMENTS WERE THE ALE IN PIXELS, MLE, MIE IN PIXELS, AIE IN PIXELS, MASKED AVERAGE INTENSITY DIFFERENCE (MAID), MJ, IJ, AND JE

Algorithm	Exp.	ALE	MLE	AIE	MIE	MAID	MJ	IJ	JE
None	b2b1	6.9	12			0.23			
	b2b3	4.9	13			0.19			
	b2b4	8.8	21			0.22			
	b2b5	8.7	19			0.26			
UL-TPS	b2b1	0.066	0.087	0.90	2.7	0.16	0.56	0.75	0.053
	b2b3	0.073	0.098	0.78	3.1	0.18	0.50	0.57	0.092
	b2b4	0.062	0.088	0.94	3.4	0.13	0.51	0.66	0.090
	b2b5	0.030	0.061	1.2	3.8	0.16	0.56	0.67	0.050
AUL-TPS	b2b1	0.016	0.029	0.0057	0.13	0.16	0.59	0.73	0.00048
	b2b3	0.017	0.053	0.0066	0.10	0.18	0.55	0.53	0.0023
	b2b4	0.030	0.065	0.0096	0.22	0.13	0.54	0.62	0.0010
	b2b5	0.031	0.046	0.0096	0.12	0.16	0.56	0.62	0.0011
CL-TPS	b2b1	0.000030	0.00011	0.0012	0.028	0.16	0.59	0.73	0.0011
20 iter.	b2b3	0.000034	0.00014	0.0016	0.022	0.18	0.55	0.53	0.0014
	b2b4	0.0083	0.083	0.079	0.42	0.13	0.54	0.62	0.0011
	b2b5	0.000006	0.00037	0.0024	0.015	0.16	0.56	0.62	0.00021
CI-TPS	b2b1	1.5	3.1	0.0045	0.048	0.097	0.26	0.47	0.011
1000 iter.	b2b3	1.6	2.9	0.0043	0.052	0.11	0.25	0.29	0.017
	b2b4	1.0	2.2	0.0040	0.063	0.084	0.26	0.44	0.0075
	b2b5	1.4	3.4	0.0044	0.099	0.092	0.18	0.32	0.0091
CLI-TPS	b2b1	1.1	2.0	0.020	0.40	0.091	0.19	0.37	0.036
300 iter.	b2b3	1.1	2.0	0.021	0.62	0.10	0.13	0.23	0.030
	b2b4	0.75	1.6	0.017	0.61	0.080	0.12	0.39	0.025
	b2b5	1.1	2.8	0.021	0.96	0.088	0.10	0.17	0.034

registration and landmark and CLI-TPS image registration. Experiments in two dimensions were used to show that the inverse consistency error between the forward and reverse transformations generated from the traditional UL-TPS could be minimized using the CL-TPS algorithm. Inverse consistency error images showed that the largest error occurred away from the landmark points for the UL-TPS algorithm and near the landmark points for the CL-TPS algorithm. The maximum CL-TPS inverse consistency error was reduced by 500 times in the inner-to-outer dots example and greater than 6 times in the 2-D MRI brain example when compared with the UL-TPS registration. The JE was reduced from 1.4 to 0.0012 for the inner-to-outer dots example and from 0.050 to 0.034 for the MRI brain example. Using landmark and intensity information with the MRI brain example gave a better intensity matching between the images than just using the landmark information as visualized in Fig. 8 and by a decrease in the average intensity difference recorded in Table III. It was shown that using both landmark and intensity information gave a better registration of the MRI brain images than using the intensity or landmark information alone.

Although the results presented in this paper are restricted to 2-D experiments, the extension of the algorithmic principles to three dimensions is straight forward. A few of the issues involved with going from 2-D to 3-D include, the 3-D implementation require more computer memory and computation time to converge, and the periodic landmark extension presented in Section II-B requires that the landmarks be replicated in 27 adjacent image domains in 3-D. Another desired improvement in going from 2-D to 3-D would be to develop an exact method for the periodic landmark registration problem to reduce memory and computational requirements when dealing with large numbers of landmarks.

APPENDIX
ESTIMATING THIN-PLATE SPLINE PARAMETERS

The unknown UL-TPS parameters $W = [\xi_1, \ldots, \xi_M, a_1, a_2, b]^T$ in (3) are determined by solving the linear system of equations that result by fixing the displacement field values at landmark locations. Let $\phi_{i,j} = \phi(|p_i - p_j|)$ and build the matrix

$$K = \begin{bmatrix} \Phi & \Lambda \\ \Lambda^T & O \end{bmatrix}$$

where

$$\Phi = \begin{bmatrix} \phi_{1,1} & \phi_{1,2} & \cdots & \phi_{1,M} \\ \phi_{2,1} & \phi_{2,2} & \cdots & \phi_{2,M} \\ \vdots & \vdots & \ddots & \vdots \\ \phi_{M,1} & \phi_{M,2} & \cdots & \phi_{M,M} \end{bmatrix}$$

$$\Lambda = \begin{bmatrix} p_1 & q_1 & 1 \\ p_2 & q_2 & 1 \\ \vdots & \vdots & \vdots \\ p_M & q_M & 1 \end{bmatrix} \tag{7}$$

where O is a 3×3 matrix of zeros. Also, define the $(M + 3) \times 2$ matrix of landmark displacements as $D = [d_1, \ldots, d_M, 0, 0, 0]^T$ where $d_i = q_i - p_i$ for $i = 1, \ldots, M$. The equations formed by substituting the landmark constrains into (3) can be written in matrix form as $D = KW$. The solution W to this matrix equation is determined by least squares estimation since the matrix K is not guaranteed to be full rank.

ACKNOWLEDGMENT

The authors would like to thank J. Haller and M. W. Vannier of the Department of Radiology, The University of Iowa, for providing the MRI data.

REFERENCES

[1] F. L. Bookstein, *Lecture Notes in Biomathematics*. New York: Springer-Verlag, 1978, vol. 24, The Measurement of Biological Shape and Shape Change.
[2] ——, *Morphometric Tools for Landmark Data*. New York: Cambridge Univ. Press, 1991.
[3] A. C. Evans, C. Beil, S. Marret, C. J. Thompson, and A. Hakim, "Anatomical-functional correlation using an adjustable MRI-based region of interest atlas with positron emission tomography," *J. Cereb. Blood Flow and Metabolism*, vol. 8, pp. 513–530, 1988.
[4] K. Rohr, M. Fornefett, and H. S. Stiehl, "Approximating thin-plate splines for elastic registration: Integration of landmark errors and orientation attributes," in *Information Processing in Medical Imaging*, A. Kuba and M. Samal, Eds. Berlin, Germany: Springer-Verlag, 1999, vol. 1613, LCNS, pp. 252–265.
[5] C. A. Davatzikos, J. L. Prince, and R. N. Bryan, "Image registration based on boundary mapping," *IEEE Trans. Med. Imag.*, vol. 15, pp. 112–115, Feb. 1996.
[6] J. P. Thirion, "Image matching as a diffusion process: an analogy with maxwell's demons," *Med. Image Anal.*, vol. 2, pp. 243–260, 1998.
[7] G. Subsol, "Crest lines for curve-based warping," in *Brain Warping*, A. Toga, Ed. San Diego, CA: Academic, 1999, pp. 241–262.
[8] C. A. Pelizzari, G. T. Y. Chen, D. R. Spelbring, R. R. Weichselbaum, and C. T. Chen, "Accurate three-dimensional registration of CT, PET, and/or MR images of the brain," *J. Comput. Assist. Tomogr.*, vol. 13, no. 1, pp. 20–26, 1989.

[9] P. M. Thompson and A. W. Toga, "A surface-based technique for warping three-dimensional images of the brain," *IEEE Trans. Med. Imag.*, vol. 15, pp. 1–16, Aug. 1996.
[10] N. Krahnstover and C. Lorenz, "Development of a point-based shape representation of arbitrary three-dimensional medical objects suitable for statistical shape modeling," *Proc. SPIE*, vol. 3661, pp. 620–631, 1999.
[11] J. H. Downs, J. L. Lancaster, and P. T. Fox, "Surface-based spatial normalization using convex hulls," in *Brain Warping*, A. Toga, Ed. San Diego, CA: Academic, 1999, pp. 263–282.
[12] R. Bajcsy and S. Kovacic, "Multiresolution elastic matching," *Comput. Vis., Graph. Image Processing*, vol. 46, pp. 1–21, 1989.
[13] R. P. Woods, J. C. Mazziotta, and S. R. Cherry, "MRI-PET registration with automated algorithm," *J. Comput. Assist. Tomogr.*, vol. 17, no. 4, pp. 536–546, July/Aug. 1993.
[14] M. I. Miller, G. E. Christensen, Y. Amit, and U. Grenander, "Mathematical textbook of deformable neuroanatomies," *Proc. Nat. Acad. Sci.*, vol. 90, no. 24, pp. 11 944–11 948, Dec. 1993.
[15] G. E. Christensen, R. D. Rabbitt, and M. I. Miller, "Deformable templates using large deformation kinematics," *IEEE Trans. Image Processing*, vol. 5, pp. 1435–1447, Oct. 1996.
[16] D. L. Collins, P. Neelin, T. M. Peters, and A. C. Evans, "Automatic 3D intersubject registration on MR volumetric data in standardized talairach space," *J. Comput. Assist. Tomogr.*, vol. 18, no. 2, pp. 192–205, March/April 1994.
[17] Y. Amit, "A nonlinear variational problem for image matching," *SIAM J. Scientific Computation*, vol. 15, no. 1, Jan. 1994.
[18] J. C. Gee, L. Le Briquer, C. Barillot, and D. R. Haynor, "Probabilistic matching of brain images," in *Information Processing in Medical Imaging*, Y. Bizais, C. Braillot, and R. Di Paola, Eds. Boston, MA: Kluwer Academic, 1995, vol. 3, pp. 113–125.
[19] R. P. Woods, S. T. Grafton, C. J. Holmes, S. R. Cherry, and J. C. Mazziotta, "Automated image registration: I. general methods and intrasubject, intramodality validation," *J. Comput. Assist. Tomogr.*, vol. 22, no. 1, pp. 139–152, 1998.
[20] J. Ashburner and K. J. Friston, "Spatial normalization," in *Brain Warping*, A. Toga, Ed. San Diego, CA: Academic, 1999, vol. 37, pp. 27–44.
[21] J. Ashburner, J. L. R. Andersson, and K. J. Friston, "High-dimensional image registration using symmetric priors," *NeuroImage*, vol. 9, pp. 619–628, 1999.
[22] I. L. Dryden and K. V. Mardia, *Statistical Shape Analysis*. New York: Wiley, 1998.
[23] F. L. Bookstein, "Linear methods for nonlinear maps: Procrustes fits, thin-plate splines, and the biometric analysis of shape variability," in *Brain Warping*, A. Toga, Ed. San Diego, CA: Academic, 1999, pp. 157–181.
[24] J. T. Kent and K. V. Mardia, "The link between kriging and thin-plate splines," in *Probability, Statistics and Optimization*, F. P. Kelly, Ed. New York: Wiley, 1994.
[25] S. C. Joshi, M. I. Miller, G. E. Christensen, A. Banerjee, T. A. Coogan, and U. Grenander, "Hierarchical brain mapping via a generalized Dirichlet solution for mapping brain manifolds," in *Proc. SPIE*, R. A. Melter, A. Y. Wu, F. L. Bookstein, and W. D. Green, Eds., 1995, vol. 2573, Vision Geometry IV, pp. 278–289.
[26] F. L. Bookstein and W. D. K. Green, "Edge information at landmarks in medical images," in *Proc. SPIE*, R. A. Robb, Ed., 1992, vol. 1808, Visualization in Biomedical Computing 1992, pp. 242–258.
[27] S. C. Joshi, "Large deformation diffeomorphisms and gaussian random fields for statistical characterization of brain sub-manifolds," D.Sc. dissertation, Dept. Elect. Eng., Sever Inst. Technol., Washington Univ., St. Louis, MO, 1997.
[28] M. I. Miller, S. C. Joshi, and G. E. Christensen, "Large deformation fluid diffeomorphisms for landmark and image matching," in *Brain Warping*, A. Toga, Ed. San Diego, CA: Academic, 1999, pp. 115–132.
[29] S. C. Joshi and M. I. Miller, "Landmark matching via large deformation diffeomorphisms," *IEEE Trans. Image Processing*, vol. 9, pp. 1357–1370, Aug. 2000.
[30] G. E. Christensen, S. C. Joshi, and M. I. Miller, "Volumetric transformation of brain anatomy," *IEEE Trans. Med. Imag.*, vol. 16, pp. 864–877, Dec. 1997.
[31] J. Kybic, "Elastic image registration using parametric deformation models," Ph.D. dissertation, Swiss Fed. Inst. Technol. Lausanne (EPFL), Lausanne, Switzerland, 2001.
[32] G. E. Christensen, "Consistent linear-elastic transformations for image matching," in *Information Processing in Medical Imaging*, A. Kuba and M. Samal, Eds. Berlin, Germany: Springer-Verlag, 1999, vol. 1613, LCNS, pp. 224–237.
[33] H. J. Johnson, "Method for consistent linear-elastic medical image registration," M.S. thesis, Dept. Elect. Comput. Eng., Univ. Iowa, Iowa City, IA, 2000.
[34] G. E. Christensen and H. J. Johnson, "Consistent image registration," *IEEE Trans. Med. Imag.*, vol. 20, pp. 568–582, July 2001.
[35] J. Talairach and P. Tournoux, *Co-Planar Stereotactic Atlas of the Human Brain*. Stuttgart, Germany: Beorg Thieme Verlag, 1988.
[36] U. Grenander and M. I. Miller, "Computational anatomy: An emerging discipline," *Quart. Appl. Math.*, vol. LVI, no. 4, pp. 617–694, Dec. 1998.
[37] A. Toga, Ed., *Brain Warping*. San Diego, CA: Academic, 1999.
[38] H. J. Johnson, "Image registration methods for the synthesis and evaluation of anatomical population summaries," Ph.D. dissertation, Dept. Elect. Comput. Eng., Univ. Iowa, Iowa City, IA, 2000.